Effectiveness of the MCC Method in Detecting Oceanic Circulation Patterns at a Local Scale from Sequential AVHRR Images

Jay Gao and Matthew B. Lythe

Abstract

The maximum cross-correlation coefficient (MCC) method is a recently devised automatic approach for detecting translational motions from remotely sensed data, and has been commonly used to estimate motion velocities. This paper aims to evaluate the effectiveness of this method in detecting oceanic circulation patterns on a local scale from sequential AVHRR images. It is found that the MCC-derived results from one image pair are indicative of the general flows only. Incoherent flows caused by non-translational motions result in the detected circulation pattern being in loose agreement with the cruising-observed circulation pattern (COCP). Averaging of the directions detected from multiple image pairs slightly improves this agreement. The main factors constraining the performance of the MCC method are identified as rotational and strained motions, isothermal fields, and non-advective processes. Their impact is drastically minimized if the detected results are tested at a significance level of 90 percent or higher. Their elimination from the flow fields causes the retained directions to be more uniform. The larger the number of images used in a detection, the closer the correlation of the detected results with the COCP, especially at a higher significance level. The flow field averaged from three pairs and tested at the 99 percent significance level is most closely correlated with the COCP at a coefficient of 0.728 that is underestimated by 8 percent due to the quality of the COCP.

Introduction

It is important to understand oceanic circulation patterns in a region because of their direct effect on the climate and socioeconomic activities in the immediate vicinity. Conventionally, oceanic flow directions are detected through manual comparison of sequential remote sensing images (Tanaka *et al.*, 1982; Vastano and Border, 1984). Although very simplistic and easy to implement, this method of detection is severely constrained by the requirement of an invariant feature (e.g., an eddy) that may not exist in all images. Moreover, the detected results are remarkably subjective because the selection of the feature varies with the analyst. Recently, two objective methods have been devised to improve detection. The first involves computation of temporal sea surface temperature (SST) derivatives from meteorological satellite data (Kelly, 1989). The success of this approach is dependent largely upon the quality of the SST data and is, thus, not studied in this paper.

The second objective approach developed by Emery *et al.* (1986) for time-sequential Advanced Very High Resolution Radiometer (AVHRR) images involves the calculation of all possible cross-correlation coefficients between a sub-area in the first image and its corresponding templates within a search window in the second time-lagged image. Under the assumption that the entire feature to be detected moves only translationally, the location of the maximum cross-correlation coefficient (MCC) in the second template is considered to be the displaced position of the feature. Since its emergence, this method has been applied to determining the velocities of such moving features as ocean currents, icebergs, and cloud (Garcia and Robinson, 1989; Kamachi, 1989; Wu *et al.*, 1992). Garcia and Robinson (1989) computed current velocities in the English Channel from sequential Coastal Zone Color Scanner (CZCS) images. Using AVHRR images, Kamachi (1989) studied surface velocity fields in the Kuroshio Current, Japan. Wu *et al.* (1992) determined advective velocities from AVHRR-derived SST images over the Chatham Rise. Liu and Yang (1994) computed surface velocities from AVHRR data in the East China Sea. Additionally, the MCC method was used to detect cloud motions (Leese *et al.*, 1971) and to determine the displacement of pack ice (Ninnis *et al.*, 1986). All these authors demonstrated that the MCC-derived results were in strong agreement with existing knowledge of surface flow velocities in the regions studied.

Limited research has been undertaken to quantitatively assess the effectiveness of the MCC method in estimating sea surface velocities from satellite images. Tokmakian *et al.* (1990) evaluated its performance using synthetic AVHRR and CZCS images. They found that the estimated velocities are more reliable if the pairs are separated by 12 hours or less and the results from several pairs are averaged. No research has been carried out to evaluate the effectiveness of the MCC method in detecting patterns of oceanic circulation at a local scale.

The principal objective of this research is to evaluate the utility of the MCC approach in detecting oceanic circulation patterns at a micro-scale off the east coast of the North Island, New Zealand from AVHRR-derived SST images. Circulation patterns detected from three pairs of sequential SST images are evaluated and compared with the geostrophic patterns obtained from cruising observation. Factors critical to

J. Gao is with the Department of Geography, University of Auckland, Private Bag 92019, Auckland, New Zealand (jg.gao@auckland.ac.nz).

M. B. Lythe is with the International Center for Antarctic Information and Research, P.O. Box 14-199, Christchurch, New Zealand.

Photogrammetric Engineering & Remote Sensing, Vol. 64, No. 4, April 1998, pp. 301–308.

0099-1112/98/6404–301$3.00/0

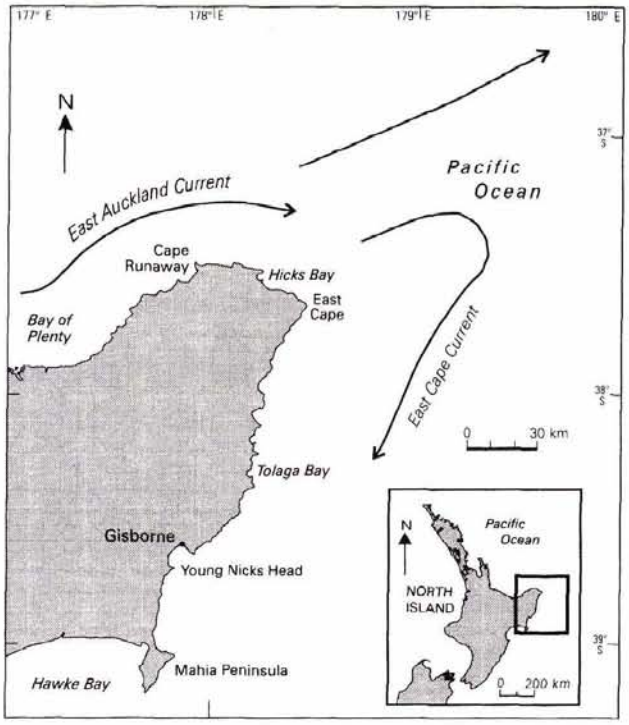

Figure 1. Location of the study area.

the success of the MCC approach are identified by the comparison and by their potential impact on the detected patterns assessed.

Study Area

Coastal waters off the East Cape peninsula (Figure 1) have been selected for this study because of the regular and definite patterns of circulation there. This area ranges from 36°30'S to 39°30'S in latitude and from 177°E to 180°E in longitude. It encompasses a large portion of Bay of Plenty and Hawke Bay, with land accounting for 18 percent of the total area. Sheltered by the high country in the North Island, the area has a sunny, calm climate with comparatively frequent dry spells. Wind velocities rarely exceed 25 $kmhr^{-1}$ (Thompson, 1987). The most recurrent winds are west or southwest in the western Bay of Plenty and southern Hawke Bay. Northwest winds are the most common around the East Cape peninsula and Gisborne. Northerly sea breezes of 20 to 30 $kmhr^{-1}$ may develop in coastal waters on fine summer days if the pressure gradient is small. Surface water temperatures in the area vary between 18 to 23°C during January-March and 14 to 18°C in July. Due to the presence of a strong thermocline, the horizontal temperature gradient in summer is larger than in winter.

The circulation pattern in the study area is controlled by the East Auckland Current. It circulates southeastward before reaching eastern Bay of Plenty where it divides into two distinctive parts. North of 37°S the first component is directed east and contributes to a counterclockwise flow of subtropical water near 180°. South of 37°S the second component turns clockwise around East Cape and gives rise to the East Cape Current.

Data Used

The AVHRR data used in this research were received directly from the National Oceanic and Atmospheric Administration (NOAA) satellite by a tracking antenna on the Landcare Research building at Gracefield, Wellington. They were transmitted by the NOAA-11 satellite passing the study area around 0400 and 1600 New Zealand Standard Time daily. Temperatures derived from the AVHRR images were recorded at 8 bits and had a resolution of 0.125°C. Recorded between April 1989 and January 1994 and resampled to a pixel size of 60 arc seconds, 2456 AVHRR scenes were collected, each having a size of 180 by 180 pixels. These were imported to ERDAS Imagine and displayed for visual inspection of cloud coverage. Containing substantial oceanographic information, 17 pairs of images were analyzed. All had a temporal separation of approximately 12 hours. Recorded on 5 February (1525 GMT), 6 February 1991 (0247 GMT), 7 March 1990 (0212 and 1338 GMT), and 11 March 1992 (0306 and 1422 GMT), three pairs of images were used for this evaluation. Their selection was based on the availability of Cruising-Observed Circulation Pattern (COCP) recordings from the same time frame. Cloud coverage was 8 percent in the 7 March and 6 February images, but absent from the remaining three. The use of a number of ground control points (GCPs) allowed the images to be transformed to the latitude-longitude coordinate system.

The MCC Method

In the MCC method a thermal feature detected in the first image may move in any direction at any magnitude in the second time-lagged image. Its displaced position is searched within a window centered at its current position in the second image (Figure 2). There is a cross-correlation coefficient between the two images for every template inside the search window. The position of the maximum cross-correlation coefficient is considered the end point of the motion. In order to eliminate random correlation caused by noise or non-translational motions, the detection is usually followed by a significance test. If a correlation coefficient exceeds a user-specified threshold, the spatial displacement between the two subareas is considered to represent a genuine motion.

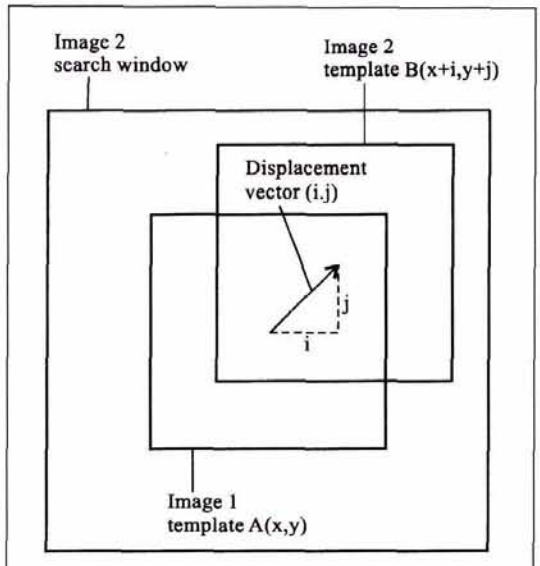

Figure 2. Relationship between template $A(x,y)$ in Image 1 and template $B(x+i,y+j)$ in Image 2. Taken from the centroid of both templates, vector (i,j) represents a potentially genuine displacement.

The entire process is composed of four steps: (1) determination of a spatial scale for thermal features, (2) removal of non-water pixels, (3) calculation of cross-correlation coefficients, and (4) significance test on the detected directions of movement.

Determination of Spatial Scale

The prerequisite of effectively determining the position of the displaced oceanic feature is the selection of the appropriate scale at which it occurs and has moved. A fine scale does not allow the displaced feature to be detected whereas a broad scale causes the amount of computation to increase exponentially. Visual inspection of the SST images revealed that thermal variability inside the study area occurs at a spatial scale less than 20 pixels. Thus, a template size of 20 by 20 pixels was deemed appropriate. Because resolution should be half or less of the smallest feature, a 40-pixel feature is resolved by 20 pixels. At this size the 180- by 180-pixel scene forms 8 by 8 templates, each corresponding to a search window of 40 by 40 pixels in the second image.

Removal of Contaminated Pixels

In order to avoid generating artificially large correlation coefficients for non-water pixels, pixels contaminated by land and cloud were excluded. They were identified on the basis of daily variation in their values. Both land and cloud are colder than water in a nighttime image and appear darker. In a daytime image, cloud remains darker but land brighter (warmer). In contrast, ocean surface temperature is very stable and has a narrower range of values. The upper and lower thresholds for contaminated pixels were determined through a careful examination of breakpoints in the histograms of the images. The contaminated pixels outside the thresholds were removed from the scene after a masking processing.

Calculation of Cross-Correlation Coefficients

Cross-correlation coefficient measures the linear correlation between two time-lagged SST images. The coefficient value ρ at pixel (i,j) in the two-dimensional matrix is calculated as

$$\rho(i, j) = \frac{\text{cov}[A(x,y), B(x + i, y + j)]}{\sqrt{\text{var}[A(x,y)]^* \text{ var } [B(x + i, y + j)]}} \quad (1)$$

where $A(x,y)$ stands for a pixel in the first template centered at (x,y) in Image 1 and $B(x+i,y+j)$ is its corresponding counterpart inside the search window in Image 2. Both represent the same feature separated by a displacement vector (i,j) (Figure 2). Taken from the centroid of each template, the vector (i, j) represents a genuine motion of a thermal feature only when its coefficient is the largest in the matrix. In this case its row and column indices are retained; cov and var are the covariance and variance of the two templates, respectively. They are calculated from Equations 2, 3, and 4. More information on the MCC method and its implementation is contained in Gao and Lythe (1996).

$$\text{cov}\{A(x,y),B(x+i,y+j)\} = \sum_{i=1}^{20}\sum_{j=1}^{20}[(A(x, y) - \overline{A})(B(x + i, y + j) - \overline{B}(i, j))] \quad (2)$$

$$\text{var}[A(x,y)] = \sum_{x=1}^{20}\sum_{y=1}^{20}[A(x,y) - \overline{A}]^2 \quad (3)$$

$$\text{var}[B(x + i, y + j)] = \sum_{i=1}^{20}\sum_{j=1}^{20}[B(x + i, y + j) - \overline{B}(i,j)]^2 \quad (4)$$

Significance Test

Some of the detected flow directions may not differ statistically from those randomly sampled from an uncorrelated population, and have to be eliminated. Removal is achieved by means of a significance test. The threshold $\rho(i,j)$ that is considered significant is inversely related to the mean isotropic scale (L) of an image's autocorrelation matrix. Characterized by a central peak value of 1, this matrix is derived by replacing $B(x+i,y+j)$ in Equation 1 with $A(x+i,y+j)$. L is the averaged bounds of the positive bias associated with the peak, or zero-crossing scale in the x and y directions (Lx and Ly). The mean of Lx and Ly is used to estimate the degrees of freedom (DOF) for the detected flows. In order to increase the accuracy of L, autocorrelation matrices were calculated from two images of different variances. Division of the number of pixels in a template (400) by the combined isotropic scale (9.78) yields a DOF value of 41, at which a $\rho(i,j)$ value of 0.254 is considered significant at the 90 percent level, of 0.301 at the 95 percent level, and of 0.393 at the 99 percent level, all of them being modified t values (Fisher, 1970).

Results

Identified Flow Patterns

The detected flow direction in a cell is represented by an arrow drawn from its start row and column to its end row and column. The flow field derived from the February image pair is extremely incoherent, with an indistinct easterly flow immediately north of 38°S (Plate 1, A). The flows further north are not dominated by a particular direction. A circular feature that has an eastward flow in its upper half, but a vaguely westward flow in its lower part, lies south of 38°S. These flows suggest a clockwise rotational circulation. In general, the flow field to the east of East Cape is chaotic without a dominant direction. This flow pattern changes considerably in the 7 March result. Incoherent flows are confined to north of 38.5°S where the temperature is spatially similar (Plate 1, B). Flows south of 38.5°S are towards the general direction of southeast, south, and southwest. However, those around 39°S are incoherent and without a predominant direction. The 11 March circulation pattern is more uniform with a number of conflicting flows (Plate 1, C). The most coherent flow occurs to the immediate north of East Cape where it is definitely southeastward. Flows north of 37°S are arguably eastward.

The start and end row and column indices of a detected flow in the ith cell were converted to its orientation θ_{id}, referenced clockwise from the magnetic north, using Equation 5: i.e.,

$$\theta_{id} = \begin{cases} 180 - \tan^{-1}(\Delta C / \Delta R)(\Delta R \geq 0, \Delta C > 0) \\ 180 + \tan^{-1}(-\Delta C / \Delta R)(\Delta R > 0, \Delta C \leq 0) \\ \tan^{-1}(-\Delta C / \Delta R)(\Delta R < 0, \Delta C \geq 0) \\ 360 - \tan^{-1}(\Delta C / \Delta R)(\Delta R \leq 0, \Delta C < 0) \end{cases} \quad (5)$$

where $\Delta C = C_{ie} - C_{is}$ and $\Delta R = R_{ie} - R_{is}$. C_{ie} and R_{ie} stand for the ith end column and row numbers of the flow; C_{is} and R_{is} are its start column and row numbers.

Not counting the grid cells contaminated by land or cloud, there are 46, 48, and 47 valid flows in the February, 7 March, and 11 March results, respectively (Table 1). They were categorized into 16 groups at an interval of 22.5°. Although flows of nearly all directions are represented in the February result, they are highly concentrated within 90 to 112.5°. Of the 46 flows, 23, or 50 percent, fall into the 45 to 135° range. In contrast, flows in the remaining directions are subordinate, especially the north-related ones. This distribution is slightly altered in the 7 March result. The number of flows in the most dominant range is drastically reduced from ten to six. Instead, the number of flows in its neighboring

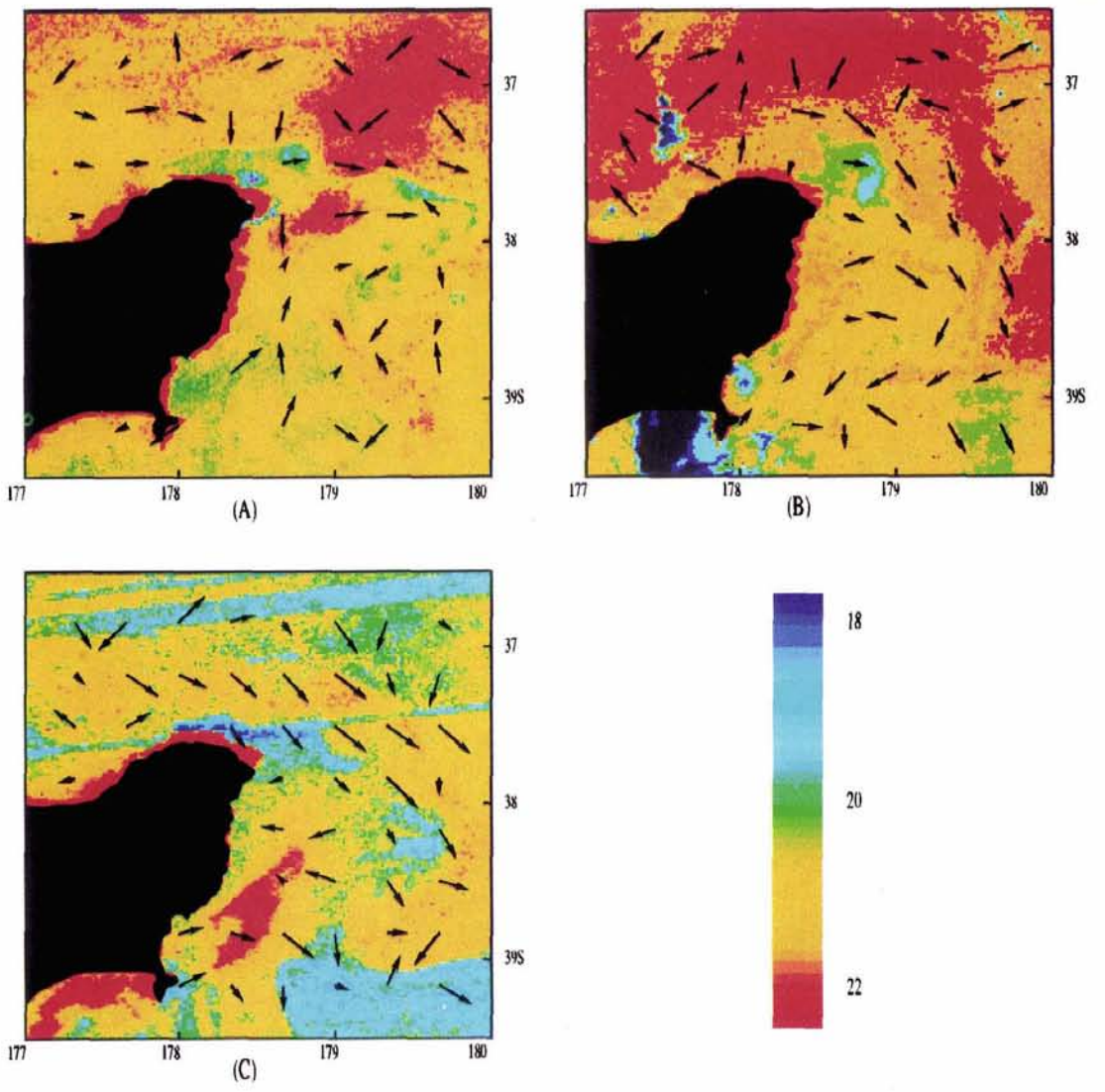

Plate 1. MCC-derived flow fields superimposed over daytime images. Flow directions are drawn from start row and column indices of a displaced feature to its end row and column numbers. Temperatures are in degrees Celsius. (A) from 5 February [1525 GMT] and 6 February [0247 GMT] 1991 image pair; (B) from 7 March 1990 [0212 and 1338 GMT] image pair; and (C) from 11 March 1992 [0306 GMT and 1433 GMT] image pair.

categories rises. The flow directions detected from the 11 March image pair are remarkably clustered, with 21 falling into the 112.5 to 157.5° range. By comparison, all other ranges contain only a few flows.

Correlation with COCP

Although indicative of the general flows in the study area, the MCC-derived field contains inconsistent and contradictory directions that are not characteristic of geostrophic flow. Its accuracy was evaluated in a per-direction based comparison with the COCP (Figure 3) obtained in February/March 1969 (Heath, 1975). A transparent grid of 8 by 8 cells was overlaid on top of it. Five of the 46 sampled flow directions fall inside the study area. The indicated flow lines intersect with the borders of 25 grid cells. More flow lines were interpolated so that every non-land cell could receive a section of them. The cruising-observed flow direction in a cell (θ_g) was measured with a protractor clockwise from magnetic north to the indicated flow line. The measured directions cluster in two groups, corresponding to the easterly flow north of East Cape and the southwest flow south of East Cape (Table 1).

The resemblance of the detected flow direction in the ith cell (θ_{id}) to its θ_{ig} is evaluated through their correlation coefficient ρ_i, or cosine of their disparity. The correlation (ρ) between the MCC-derived flow field and the COCP is the arithmetic mean of all the coefficients (Costanzo and Gale, 1984), or

$$\rho = \frac{1}{N}\sum_{i=1}^{N}\rho_i = \frac{1}{N}\sum_{i=1}^{N}\cos(\theta_{id} - \theta_{ig}) \qquad (6)$$

where N stands for the number of flow directions. ρ_i is calculated only when the cross-correlation coefficient $\rho(i,j)$ associated with θ_{id} is statistically significant if a significance test is applied. In case θ_{id} is averaged from multiple pairs, $\rho(i,j)$ at the ith cell must be statistically significant for all the pairs used.

TABLE 1. DISTRIBUTION OF DETECTED FLOW DIRECTIONS

Category	5/6 Feb	7 Mar	11 Mar	Observed
≤22.5	0	3	1	0
≤45	2	2	1	0
≤67.5	3	4	4	11
≤90	4	2	2	9
≤112.5	10	6	1	5
≤135	6	4	12	1
≤157.5	4	6	9	0
≤180	1	4	2	2
≤202.5	4	2	4	6
≤225	2	3	1	14
≤247.5	6	3	2	0
≤270	0	2	3	0
≤292.5	1	2	1	0
≤315	2	3	1	0
≤337.5	0	2	1	0
≤360	1	0	2	0
Sum	46	48	47	48

TABLE 2. CORRELATION COEFFICIENTS OF THE DETECTED DIRECTIONS WITH SHIP-BASED MEASUREMENTS

SST image pair(s)	No test	90%	Change (%)	95%	Change (%)	99%	Change (%)
5/6 Feb	0.256	0.260	1.6	0.295	13.5	0.408	38.3
7 Mar	0.347	0.318	−8.4	0.364	14.5	0.424	16.5
11 Mar	0.215	0.195	−9.3	0.239	22.6	0.396	65.7
(mean)	0.273	0.258	−5.4	0.299	16.9	0.409	40.2
5/6 Feb & 7 Mar	0.411	0.406	−1.2	0.507	24.9	0.536	5.7
5/6 Feb & 11 Mar	0.255	0.285	11.8	0.347	21.8	0.619	78.4
7 & 11 Mar	0.329	0.301	−8.5	0.411	36.5	0.636	54.8
(mean)	0.332	0.331	−0.7	0.422	27.7	0.597	46.3
5/6 Feb & 7, 11 Mar	0.371	0.401	8.1	0.595	48.4	0.728	22.4
Significance level		0.254		0.301		0.393	

The individual coefficients ρ_i range from −0.999 to 1.000 for the February result. Of the 45 coefficients, 13 are negative and 32 positive, their mean being 0.256 (Table 2). The negative ones are widely distributed across the scene, but have a higher concentration in the southeast corner and the upper portion of the scene. A significance test at the 90 percent level causes four random flows to be eliminated and an improvement of 1.6 percent in ρ to 0.260. As the significance level rises to 95 and 99 percent, ρ increases to 0.295 and 0.408, respectively. After the removal of the more incoherent flows in the top and the bottom of the scene, the retained ones become predominantly eastward and southward with fewer anomalies (Figure 4a).

The 7 March result contains 13 negative and 35 positive coefficients. Their maxima, minima, and mean are 0.999, −0.946, and 0.347, respectively. The negative coefficients are spatially dispersed. The mean coefficient rises to 0.318 at the 90 percent significance level. After ten statistically insignificant flows are excluded from the evaluation at the 90 percent level, ρ drops by 8.4 percent to 0.318. However, it bounces back to 0.364 and 0.424 at the 95 and 99 percent levels, respectively. Examination of the flow field (Figure 4b) reveals that these flows are located in the northwest and northeast corners where there is no dominant flow. Most of the retained directions south of East Cape are coherently southeastward and southwestward.

The 48 coefficients for the 11 March result range from −0.990 to 1.000 with a mean of 0.215. Most of the 15 negative coefficients are situated in the northeastern corner and the bottom of the scene. The mean coefficient decreases to 0.195 at the 90 percent significance level after seven flows are eliminated. With the rise of the significance level to 95 percent, six more directions become statistically insignificant. Their exclusion from the evaluation results in a larger ρ

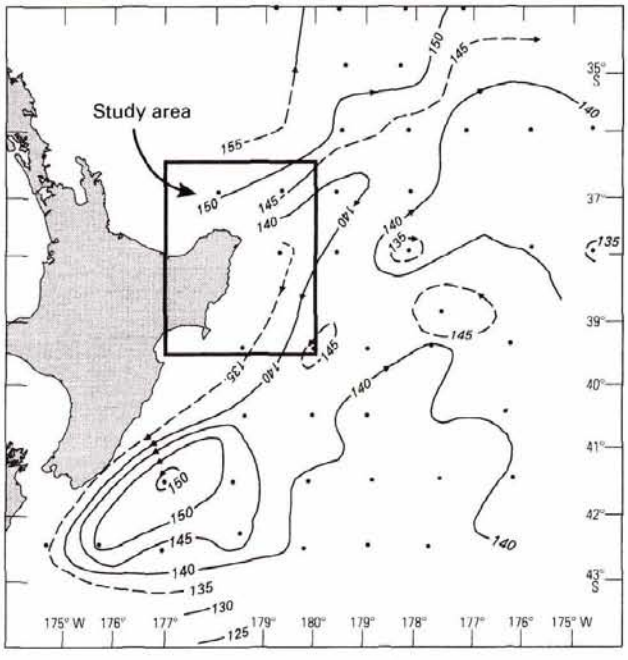

Figure 3. Flow patterns in February/March 1969 at the geopotential topography of the sea surface relative to 1000 dbars (source: Health, 1975).

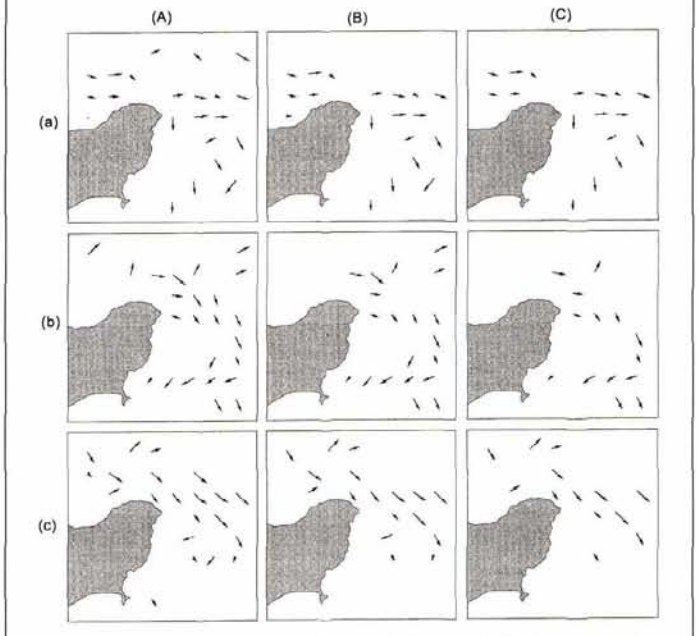

Figure 4. Flow directions detected from single image pair at three significance levels. (A) 90 percent, (B) 95 percent, and (C) 99 percent. (a) from 5/6 February image pair, (b) from 7 March image pair, and (c) from 11 March image pair.

value of 0.239. At the significance level of 99 percent, ρ reaches 0.396.

As more incoherent flows are eliminated, the MCC-derived flow field is in increasing agreement with the COCP. However, the highest agreement never exceeds 0.424. In order to achieve a higher level of agreement, flow directions detected from more than one image pair were averaged. If a grid cell under study had a valid flow in all pairs, its direction was calculated by dividing the sum of column displacement in easting by the total row displacement in northing. The three pairs were averaged in four ways, three from two pairs and one from three pairs. If all detected directions are used for evaluation, the flow directions averaged from two pairs have a correlation, on average, of 0.332 with the COCP, slightly larger than that (0.273) for unaveraged ones (Table 2). Although the correlation is hardly improved at the 90 percent significance level, its coefficient of 0.331 is still larger than the corresponding figure (0.258) for unaveraged directions. However, the correlation becomes increasingly closer after the removal of more flows at a higher significance level. For instance, the correlation rises, on average, to 0.422 at the 95 percent level, or 0.123 higher than that for unprocessed directions. At the 99 percent level, the averaged directions outperform the ones from one image pair, on average, by 46 percent.

Flow directions detected from three pairs bear slightly more resemblance to the COCP than those averaged from two pairs if all flows are included in the evaluation. However, their correlation with the COCP (0.371) is smaller than that (0.411) derived from the 6 February/7 March pair (Table 2). The advantage of using more pairs in the detection is manifested after a significant test is undertaken. For instance, the correlation increases by 8.1 percent to 0.401 at the 90 percent significance level. Although this coefficient value is the second largest among its seven counterparts at that significance level, its gap with the largest figure is only 0.005. At the 95 percent level, the correlation becomes considerably closer with a coefficient of 0.595. It exceeds all others at the same significance level. At the 99 percent level, the correlation reaches the maximum value of 0.728.

The MCC-derived flow field from one pair of SST images bears limited resemblance to the COCP. Even if the directions are averaged from multiple pairs, the resemblance is not remarkably improved because of the existence of incoherent flows. At the significance level of 90 percent, four coefficients become smaller and three larger (Table 2). The decreasing coefficients are associated with the directions detected from both one and two pairs. Therefore, this significance level is not stringent enough to eliminate some random flows that markedly affect the overall correlation. At the 95 percent significance level, the correlation increases, on average, by 16.9 percent for the directions detected from one pair, and by 27.7 and 48.4 percent for those averaged from two and three pairs, respectively. Thus, the more pairs used, the closer the correlation between the detected directions and the COCP. At the 99 percent level, the increase rate is 40.2 and 46.3 percent for the directions detected from one and two pairs, respectively. By comparison, the increase rate for the results from three pairs is only 22.4 percent because more flows have been eliminated at the previous significance level. The more pairs used in the detection, the more random flows fail the test, especially at a higher significance level. For instance, the number of retained flows decreases by more than half at the 90 percent level and by over two-thirds at the 99 percent level in all three results (Figure 4). The 90 percent significance level is ineffective in eliminating random flows. A confidence level of 95 percent is required to eliminate them if the flow directions are averaged from three pairs and 99 percent if from two pairs.

Discussion

The highest agreement between MCC-derived flow field with the cruising-determined geostrophic pattern never exceeds 0.728 in spite of the number of image pairs used and the significance level. Such a disparity is attributable to the limitations of the MCC method and the quality of the COCP used in the evaluation.

Limitations of the MCC Method

In the MCC method, it is implicitly assumed that thermal oceanic features move translationally, that they have a detectable temperature gradient, and that the changes in surface temperature are caused solely by displaced oceanic features. In practice, these assumptions are occasionally violated. Besides translational motions, there are also rotational and strained motions. Non-advective processes such as insolation-related warming also alter the surface temperature regime.

Rotational and Strained Motions

The MCC method requires flexibility in searching for neighboring pixels and uniformity in the advective flow field. If the size of a template or search window is fixed as in this study, it is unable to detect rotational and strained motions. However, these motions are not absolute, and can be approximated as translational motions if the spatial and temporal scales are sufficiently small (Wu *et al.*, 1993). Because the pairs used in this study have a temporal separation of around 12 hours, the errors caused by the approximation are tolerable (Tokamakian *et al.*, 1990). The impact of the rotational flow located to the east of East Cape in the 6 February image is explored by averaging the 16 coefficients inside/around the circular feature. Their mean of 0.361 is smaller than 0.378 and 0.610, the means of the same 16 coefficients in the 7 March and 11 March results, respectively. In spite of their causing a degenerated flow field, rotational flows are statistically insignificant at the 99 percent level and thus are eliminated (Figure 4a, C).

Compared with rotational motions, strained motions are much more difficult to identify in the images. It is even harder to assess the errors caused by them. The development of deformational motions depends on the stability of the advective flow field, which is, in turn, determined by the wind field at the time of imaging. Because the AVHRR data were recorded under a mostly clear sky, anticyclonic conditions must be prevalent at the time of imaging. Therefore, the detected flow field is controlled primarily by geostrophic winds with few strained motions.

Isothermal Fields

Although calm anticyclonic conditions do not favor the development of deformational motions, they are conducive to the formation of isothermal fields at a local scale. Due to the lack of a temperature gradient, definite thermal features may be absent from an isothermal field. Around 37°S, where bathymetry exerts little control over surface flow, ocean temperature is spatially less variable than elsewhere in the March 7 image (Plate 1, B). In this part of the scene the detected flows have a diverse range of directions. Because temperatures in all cells are close to one another, there is a larger chance for these directions to be random. On the one hand, the 16 coefficients in the isothermal field have a mean of 0.394, against the mean of 0.378 for 16 other coefficients in thermally heterogeneous fields of the same scene. On the other hand, the 16 coefficients located in the same position in the 6 February and 11 March results have a mean of 0.111 and 0.244, respectively. Therefore, the detected flow directions in the isothermal field are not less strongly correlated with the COCP than are those in thermally heterogeneous

fields. More importantly, these flows are insignificant and are removed at the 99 percent significance level, hence not affecting the final pattern (Figure 4b, C).

Non-Advective Processes

In addition to displaced thermal features, non-advective near surface processes also modify the SST regime. They include insolation warming, cloud cooling, and vertical mixing. Surface warming by intense insolation leads to patchy areas of anomalously high temperature (Plate 1, C). Due to the small size of these areas, this non-advective process has a minimal impact on the entire flow field. Although masking was applied to exclude the pixels contaminated by cloud from the detection, it was unable to eliminate those partially contaminated pixels. Both the 7 March images contained 8 percent of cloud cover. However, their result is more closely correlated with the COCP than those from other pairs (Table 2). Thus, cloud-related surface cooling at the sub-pixel level has a negligible impact on the detected flow fields. Topographically induced upwelling is responsible for the lowered SST between 178 and 179°E north of East Cape (Plate 1, A). Consequently, the flows around this cool patch are inconsistent with the surrounding ones, and eliminated at the 90 percent significance level (Figure 4a, A).

With only three pairs analyzed, it is impossible to quantify the impact of each of these factors. Figure 4 demonstrates that the flows associated with these factors are incoherent and insignificant as exemplified by those in the rotational and isothermal fields. Their influence is drastically minimized in a significance test at the 90 percent confidence level or higher. Significance test at the 99 percent level can improve the correlation with the COCP by, on average, 50 percent for the results detected from one pair, 80 percent for those from double pairs, and 96 percent for those from triple pairs.

Quality of COCP

The quality of the COCP used in the evaluation has four components:

- *Reliability.* It is costly to sample flow directions from a cruising ship in spite of their high reliability. Limited sampling is usually carried out to minimize the cost. The study area of nearly 40,000 km² in size encompasses only five observations. Inevitably, the indicated flow lines interpolated from such a highly limited number of observations involve a fair degree of uncertainty.
- *Scale.* Mapped at the regional scale, the COCP does not contain minor flow features taking place at the local scale. During interpolation for the flow direction in a grid cell from the indicated flow lines, more uncertainty was introduced. The differential levels of circulation detail shown in the two flow fields undoubtedly weaken their correlation. This difference explains in part why the correlation becomes stronger after the flow fields are generalized by averaging.
- *Data Misregistration.* In this vast ocean area, few definite features can be used as reliable GCPs for image rectification. Residuals in the geometrically rectified SST images could be as large as one pixel (Wahl and Simpson, 1990). Thus, a flow in the MCC field may not be the identical one located in its corresponding position in the COCP because of misregistration.
- *Changed Flow Field.* At a local scale the flow pattern, especially the residual circulation in the study area, is highly susceptible to wind stress. The weak correlation between the flow fields detected from different pairs (Table 3) suggests that at a local scale the flow pattern is dependent highly upon the weather conditions. Wind patterns at the time of imaging differed from those on the days of cruising measurement. Apart from seasonal variation in the circulation pattern, there is also interannual fluctuation in the pattern. Averaging of flow directions from multiple pairs smoothes out wind peculiarities on individual days and makes the wind regime more similar to that on the days of cruising observation. As a matter of fact, averaging of results from the individual pairs also improves the accuracy of detected current velocities estimated with the MCC method (Tokmakian *et al.*, 1990).

TABLE 3. CORRELATION COEFFICIENTS AMONG THE DETECTED RESULTS ON DIFFERENT DATES

SST Image Pairs	No Test	90%	95%	99%
5/6 Feb & 7 Mar	0.177	0.138	0.246	0.413
5/6 Feb & 11 Mar	0.204	0.370	0.297	0.543
7 & 11 Mar	0.141	0.131	0.265	0.372
(mean)	0.174	0.213	0.269	0.443

The errors caused by these factors are revealed through a comparison of the coefficients in Tables 2 and 3. If no significance test is applied, the flow pattern detected from one pair is more strongly correlated with the COCP than with that from another pair. Such a relationship holds true until the significance level reaches 99 percent except for that (0.370) of the February/11 March pair at the 90 percent level (Table 2). At the 99 percent significance level, the flow pattern detected from one pair has a looser correlation with the COCP than with that from another pair. Therefore, the limitations of the MCC-method are principally responsible for the low coefficients at the significance levels below 99 percent. The quality of the COCP becomes more important after the insignificant flows are eliminated at the 99 percent level, at which the mean (0.443) of the three coefficients (Table 3) is slightly larger than its counterpart of 0.409 (Table 2). The correlation is underestimated by 8 percent due to the limited quality of the COCP.

Conclusions

The success of the MCC method in detecting oceanic circulation patterns at a local scale relies, to a large extent, on knowledge of the nature of the thermal variance. With a properly selected spatial scale, the circulation pattern derived from the sequential AVHRR pairs separated by 12 hours is in broad agreement with the COCP. The major discrepancy between the two patterns lies in flow uniformity in the MCC-derived fields which contain a wide range of flow directions. Some of them are related to non-translational motions. Because of their presence in the fields, the MCC-derived flow pattern and the COCP are loosely correlated, with the largest coefficient being 0.371, even if the results are averaged from multiple pairs. Flows caused by non-translational motions tend to be statistically insignificant and are eliminated in a significance test that is critical to the success of the MCC method. The removal of these incoherent flows from a detected flow field enhances its uniformity and causes it to have a higher degree of agreement with the COCP. The higher the confidence level, the higher the degree of agreement. On average, the correlation becomes 17 and 40 percent closer for the results detected from one pair as the significance level rises, respectively, from 90 to 95 percent, and from 95 to 99 percent. The corresponding rates are 30 and 46 percent for the results averaged from two pairs, and 50 and 22 percent for those averaged from three pairs. At the same significance level, the more pairs used in a detection, the more closely the detected results are correlated with the COCP. At the 99 percent significance level, the flow pattern detected from three pairs is in close agreement with the COCP, with a correlation coefficient of 0.728. This value is underestimated by about 8 percent due to the quality of the COCP used in the evaluation.

Although the MCC method is unable to detect rotational flows, this inability is largely overcome by using image pairs

separated by about 12 hours. In this way, the rotational flows are approximated as translational ones with minimal approximation errors. By comparison, strained motions causes larger errors due to the transient nature of many thermal features in the study area. Although the temperature gradient in isothermal fields is very small, the detected flows in the fields are not less closely correlated with the COCP than those in thermally heterogeneous fields. Non-advective processes such as insolation-related warming, cloud cooling, and topographically induced upwelling have little impact on the detected flow fields because of the small scale at which they take place. Their impact on the results is virtually non-existent if they are detected from three pairs and tested at the 99 percent significance level.

Acknowledgments

This research was supported by a grant from the University of Auckland Research Committee. We appreciate the assistance rendered by Anna Romaniuk in importing the data into ERDAS Imagine and in preparing the color illustration. Jonette Surridge drew Figures 1 and 3.

References

Costanzo, C.M., and N. Gale, 1984. Evaluating the similarity of geographic flows, *Professional Geographer*, 36(2):182–187.

Emery, W.J., A.C. Thomas, M.J. Collins, W.R. Crawford, and D.L. Mackas, 1986. An objective method for computing advective velocities from sequential infrared satellite images, *Journal of Geophysical Research*, 94(C11):12865–12878.

Fisher, R.A., 1970. *Statistical Methods for Research Workers*, Oliver and Boyd Ltd, Edinburgh, 362 p.

Gao, J., and M.B. Lythe, 1996. The maximum cross-correlation approach to detecting translational motions from sequential remote-sensing images, *Computers & Geosciences*, 22(5):525–534.

Garcia, C.A.E., and I.S. Robinson, 1989. Sea surface velocities in shallow sea extracted from sequential Coastal Zone Color Scanner Satellite Data, *Journal of Geophysical Research*, 94(C9): 12681–12691.

Heath, R.A., 1975. *Oceanic Circulation off the East Coast of New Zealand*, New Zealand Oceanographic Institute Memoir 55, Department of Scientific and Industrial Research, Wellington, 80 p.

Kamachi, M., 1989. Advective surface velocities derived from sequential images for rotational flow field — limitations and applications of maximum cross-correlation method with rotational registration, *Journal of Geophysical Research*, 94(C12):18277–18233.

Kelly, K.A., 1989. An inverse model for near surface velocity from infrared images, *Journal of Physical Oceanography*, 19(12):1845–1864.

Leese, J.A., C.S. Novak, and B.B. Clarke, 1971. An automated technique for obtaining cloud motion from geosynchronous satellite data using cross correlation, *Journal of Applied Meteorology*, 10: 110–132.

Liu, C., and Y. Yang, 1994. Satellite derived tidal current over East China Sea, *Proc. of the Pacific Ocean Remote Sensing Conference*, Melbourne, Australia.

Ninnis, R.M., W.J. Emery, and M.J. Collins, 1986. Automated extraction of pack ice motion from Advanced Very High Resolution Radiometer imagery, *Journal of Geophysical Research*, 91(C9): 10725–10734.

Tanaka, S., T. Sugimura, T. Nishimura, Y. Nonomiya, and Y. Hatakeyama, 1982. Compilation of the Kuroshio Current vector map from NOAA-6/AVHRR data and consideration of ocean eddies and the short period fluctuation of the Kuroshio, *Journal of the Remote Sensing Society of Japan*, 2:11–32.

Thompson, C.S., 1987. *The Climate and Weather of Hawke's Bay*, New Zealand Meteorological Service Miscellaneous Publication 115(5), Wellington, 46 p.

Tokmakian, R., T.P. Strub, and J. McClean-Padman, 1990. Evaluation of the maximum cross correlation method of estimating sea surface velocities from sequential satellite images, *Journal of Atmospheric and Oceanic Technology*, 7:852–865.

Vastano, A.C., and S.E. Borders, 1984. Sea surface motion over an anticyclonic eddy on the Oyashio Front, *Remote Sensing of Environment*, 16:87–90.

Wahl, D.D., and J.J. Simpson, 1990. Physical processes affecting the objective determination of near surface velocity from satellite data, *Journal of Geophysical Research*, 95:13511–13528.

Wu, Q.X., D. Pairman, S.J. McNeill, and E.J. Barnes, 1992. Computing advective velocities from satellite images of sea surface temperature, *IEEE Transactions on Geoscience and Remote Sensing*, 30(1):166–176.

(Received 10 February 1997; accepted 15 July 1997; revised 21 August 1997)